Seismic phononic crystals by elastodynamic Navier equation

Dongwoo Lee,[1] Joo Hwan Oh,[2] In Seok Kang,[3] and Junsuk Rho[1,3,*]

[1]*Department of Mechanical Engineering, Pohang University of Science and Technology (POSTECH), Pohang 37673, Republic of Korea*

[2]*School of Mechanical, Aerospace and Nuclear Engineering, Ulsan National Institute of Science and Technology, UNIST-gil 50, Eonyang-eup, Ulju-gun, Ulsan, 44919, Republic of Korea*

[3]*Department of Chemical Engineering, Pohang University of Science and Technology (POSTECH), Pohang 37673, Republic of Korea*

(Received 14 July 2019; published 20 December 2019)

The phenomenon, known as a complete band gap in photonic crystals consisting of periodically arranged manmade nanostructures, caused a huge sensation in photonics. Inspired by the physical methodology, we extend it to large-scale wave propagation for seismic waves. In particular, we exploit the elastodynamic Navier equation in the medium for seismic phononic crystals to induce complete band gaps of body (*P*) and shear (*S*) waves. We also show a technique that uses weak formulation to analyze band structures. Estimation of evanescent modes by complex-valued wave vectors yields propagation length, then we redesign bulky phononic crystals to be as thin as possible. We also investigate how material properties affect the relation between propagation length and effective particle velocity. This study will contribute to seismic-resistant techniques in seismology.

DOI: 10.1103/PhysRevE.100.063002

I. INTRODUCTION

An earthquake caused by the shaking ground motion on the Earth's layer, arising from the sudden release of energy in the crust, generates seismic waves. There is no doubt that the study of seismic wave propagation is essential due to the long and short return periods for large and small earthquakes, threatening our lives and assets. Earthquakes give rise to serious economic and social consequences to be taken into account.

Earthquake engineering is an application of multidisciplinary knowledge of how the ground motion generated by an earthquake affects typical buildings or any other manmade structures, and an application of this knowledge to design structures to withstand earthquakes. Therefore, an estimation of the expected ground motion at a particular site is required with one constraint that the cost must be minimized while assuring earthquake resistance.

Recently developed optical metamaterials and photonic crystals exploit the interaction between light and matter. For instance, negative effective parameters [1–3], metasurface cloaks [4–7], and photonic crystals [8–13] are now available in photonics. These systems consist of periodic or quasi-periodic artificial inclusions within effectively homogeneous media under the long-wavelength limit or on the relevant scale. If analogous seismic metamaterials and phononic crystals can be more developed, they may have applications in defense against seismic waves.

For instance, a seismic cloak that works in a thin plate has been proposed theoretically and numerically [14], analogous to the mechanism of an invisibility cloak with metamaterials. The cloaking structure is composed of radially symmetric multi-layers that have nearly the same mass density, but a gradual variation in Young's modulus to avoid a huge mismatch of impedance and to manipulate bending waves. Theoretical studies have suggested real materials in each layer, to be evaluated experimentally.

In particular, an earlier study of seismic phononic crystals has been experimentally reported by exploiting periodic arrangements of boreholes under the condition of the approximate Mindlin plate model [15]. Analyses of the crystal's responses suggested that Bragg scattering causes partial band gaps that are confirmed in a narrow band of frequencies along high-symmetry lines. However, in terms of first large-scale experimental works, it should be considered as the best achievement in this field so far. Another idea is to use a "natural forest via tree network" to trap Rayleigh waves. The tree network is composed of locally resonant metamaterials; it develops several band gaps with strong attenuation at the sub-wavelength scale [16]. Such a vertical alignment of rods on the substrate for seismic waves has been consequently investigated [17–19]. A gigantic work called the METAFORET project in 2018 was conducted to report the result of sub-wavelength pine-tree forests as coupled resonators that may enable attenuation of seismic surface waves [20]. Moreover, numerous other yet-unpublished suggestions that use metamaterials and phononic crystals to shield seismic waves can be obtained from arXiv [21–24]. Explicit experimental work on this topic is uncommon, because it requires large-scale samples and artificial sources to emulate the actual seismic environment. However, we believe that newly discovered approaches should extensively be used in theoretical and numerical studies of methods to confront seismic waves.

In this paper, we examine phononic crystals in seismic systems, analogous to photonic crystals in optical devices. The main governing equation that we consider is the elastic Navier's equation in homogeneous and isotropic media, which is usually used to describe seismic waves. Seismic body waves (*P*-waves) and shear waves (*S*-waves) can be

*jsrho@postech.ac.kr

readily decoupled and estimated by both analytic and numerical approaches. Specifically, we exploit a newly developed numerical technique to calculate band structures by using a weak-form-based finite element method (FEM) technique for $k(\omega)$ formulation in acoustics [25] rather than for $\omega(k)$ formulation [26–29]. We show how to implement the main equation that is not easy to apply using conventional built-in modules in a commercial FEM simulator (COMSOL MULTIPHYSICS 5.3a). To ensure that the obtained numerical solutions by weak formulation are reasonable, we also conduct an analytic approach. In order to investigate the behavior of seismic phononic crystals in the band gap, we analyze band structures for the *P*- and *S*-waves, and obtain complete band gaps with a given cylindrical design in a square unit cell. The displacement fields at several frequencies are shown to observe the band gap phenomenon. Moreover, once we know a propagation length that has not been discussed yet in existing relative researches, a bulky crystal system can be designed and simplified to a thin one. Furthermore, we discuss material properties in the band gap evaluating an effectively complex particle velocity by a parametric study of mass density, and by comparison of several materials. Results show that hard materials have a lossy component of particle velocity, so propagation length is infinitesimal in the band gap, whereas soft materials have no lossy component, so the propagation length is enormous out of the band gap.

II. ANALYTIC AND NUMERICAL SOLUTION TO ELASTIC NAVIER'S MODEL

A. Analytic solution of wave propagation

The general form of stress-strain constitutive relation by Hooke's law is written as

$$\boldsymbol{\sigma} = \mathbf{C} : \boldsymbol{\varepsilon}, \tag{1}$$

where $\boldsymbol{\sigma}$ is the stress tensor, $\boldsymbol{\varepsilon}$ is the strain tensor, and $\mathbf{C}$ is the stiffness tensor. Assuming a homogeneous isotropic medium and inserting Newton's second law yields the elastic Navier's equation as seismic waves, which we consider in this paper [30–32]:

$$\rho\ddot{\mathbf{u}} = (\lambda + 2\mu)\nabla(\nabla \cdot \mathbf{u}) - \mu(\nabla \times \nabla \times \mathbf{u}), \tag{2}$$

where ρ is the mass density, $\mathbf{u}$ is the displacement field, λ and μ are, respectively, Lamé's first and second parameters. By using Helmholtz's decomposition theorem [33] with a scalar potential Φ and a vector potential $\boldsymbol{\Psi}$ with respect to $\mathbf{u}$,

$$\mathbf{u} = \nabla\Phi + \nabla \times \boldsymbol{\Psi}, \tag{3}$$

$\mathbf{u}$ can be decoupled into two potentials. Using vector identities, and curl-free and divergence-free properties for each potential, together with gauge condition $\nabla \cdot \boldsymbol{\Psi} = 0$, Eq. (2) can be reduced to [30–32]

$$\frac{\partial^2\Phi}{\partial t^2} = \frac{(\lambda + 2\mu)}{\rho}\nabla^2\Phi, \tag{4a}$$

$$\frac{\partial^2\boldsymbol{\Psi}}{\partial t^2} = \frac{\mu}{\rho}\nabla^2\boldsymbol{\Psi}, \tag{4b}$$

where the scalar potential and the vector potential represent displacement field solutions of *P*- and *S*-waves after postprocessing, respectively. Under the assumption that each potential is a sinusoidal function of time, Eqs. (4a) and (4b) are rewritten as [30–32]

$$\left(\nabla^2 + k_p^2\right)\Phi = 0, \quad \left(\nabla^2 + k_s^2\right)\boldsymbol{\Psi} = 0, \tag{5}$$

where $k_{(\cdot)} = \omega/c_{(\cdot)}$ indicates the wave vector for the *P*- or *S*-wave, and $c_p(= \sqrt{(\lambda + 2\mu)/\rho})$ and $c_s(= \sqrt{\mu/\rho})$ are particle velocities with the angular frequency ω. To solve the Helmholtz equation and obtain the displacement field for Φ, we set $\Phi = X(x)Y(y)$ for the separation of variables. Then Eq. (5) for the two-dimensional case can be reduced to coupled ordinary differential equations as

$$\frac{1}{X}\frac{d^2X}{dx^2} = -\left(k_p^2 - \lambda_m^2\right), \tag{6a}$$

$$\frac{1}{Y}\frac{d^2Y}{dy^2} = -\lambda_m^2, \tag{6b}$$

where λ_m^2 is a separation constant and m is a mode number such that $\lambda_m = 0$ for the first mode ($m = 1$) to accomplish plane-wave-like propagation along a certain direction. Here, Eqs. (6a) and (6b) are solved with boundary conditions that are assumed to be as follows:

$$\Phi|_{x=0} = 1 \quad \text{(Dirichlet condition)}, \tag{7a}$$

$$\Phi'\big|_{x=L} = 0 \quad \text{(Neumann condition)}, \tag{7b}$$

$$\Phi'\big|_{y=0} = 0 \quad \text{(Neumann condition)}, \tag{7c}$$

$$\Phi'\big|_{y=L} = 0 \quad \text{(Neumann condition)}, \tag{7d}$$

where L is the interval length on the spatial dimension. After applying the boundary conditions to Eqs. (6a) and (6b), then the potential solution can be obtained as

$$\Phi = A\cosh\left(\sqrt{\lambda_m^2 - k_p^2}\,x\right) + B\sinh\left(\sqrt{\lambda_m^2 - k_p^2}\,x\right), \tag{8}$$

where $A = 1$, $B = -\tanh\left(\sqrt{\lambda_m^2 - k_p^2}\,L\right)$, and $\lambda_m = \lambda_1 = 0$.

Before seismic waves are considered, we could seek, for instance, the pressure field P as is computed in a solution for acoustic waves with $c_a = 343$ m/s and $L = 25$ mm in two-dimensional (2D) space [Figs. 1(a) and 1(b)]. In Eqs. (6a) and (6b), the ordering index m is truncated by an integer N, however, the mixture modes by a superposition along N is not considered here, because we consider the phononic regime in which the wavelength becomes comparable to the size of a single crystal. Therefore, in this study, we only consider the fundamental harmonic ($m = 1$) that has the lowest frequency (the longest wavelength) of a sinusoidal waveform, and has a known fixed single frequency. In this case, the solution of acoustic pressure field itself represents the scalar potential, unlike the displacement fields of seismic waves. In particular, the pressure field solutions by both analytic and numerical approaches agreed well along frequencies from 10 to 50 kHz [Fig. 1(b)].

For the vector potential, we simply consider that the *S*-wave is a shear horizontal (SH) wave, so that it is horizontally polarized with respect to the propagation direction [Fig. 1(c)]. Then it gives rise to only a y-directional displacement component $(0, u_s, 0)$ and $\nabla \cdot \mathbf{u} = 0$ arising from $\partial u_s/\partial y = 0$.

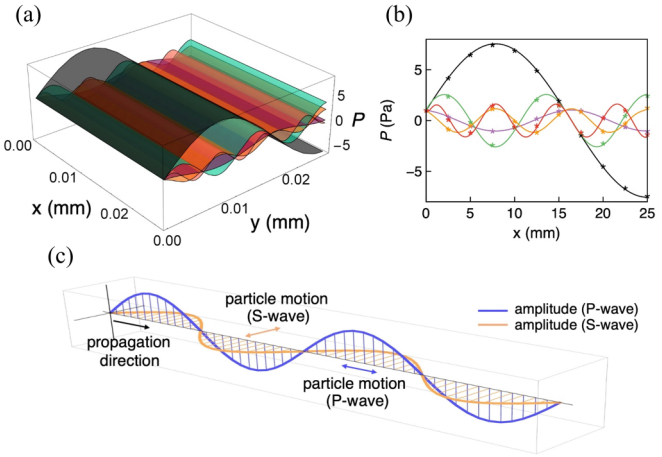

FIG. 1. (a) Pressure field in 2D space obtained by the analytic approach. (b) Analytic solutions (solid line) of pressure field in comparison with numerical solutions (asterisk) using weak formulation at 10 kHz (black), 20 kHz (violet), 30 kHz (green), 40 kHz (orange), and 50 kHz (red). (c) Schematic of a seismic wave, which consists of a *P*-wave and an *S*-wave.

Therefore, Eq. (2) simplifies to

$$\left(\nabla^2 + k_s^2\right)u_s = 0, \tag{9}$$

where $\mathbf{\Psi}$ in Eq. (4b) is replaced with u_s for the transverse motion. In the next subsection, numerical solutions by weak formulation will be introduced and compared to analytic solutions of two displacement fields.

B. Numerical solution of wave propagation through weak formulation

Here, we consider the elastodynamic Navier equation in a weak variational form and evaluate the displacement field solutions. The strong form of the *P*-wave in Eq. (5a) can be formulated imposing a functional F as an integral sense:

$$F(\Phi, \varphi) = \int_\Omega \varphi\left(\frac{1}{\rho}\nabla^2 + \frac{\omega^2}{(\lambda + 2\mu)}\right)\Phi \, d\Omega = 0, \tag{10}$$

where φ is a test function which is assumed to be smooth and compact in the domain Ω. Using the integration by parts, we can rewrite Eq. (10) as

$$F(\Phi, \varphi) = \int_\Omega \left[\nabla \cdot \left(\frac{1}{\rho}\varphi\nabla\Phi\right) - \frac{1}{\rho}\nabla\varphi \cdot \nabla\Phi + \varphi\frac{\omega^2}{(\lambda + 2\mu)}\Phi\right]d\Omega = 0, \tag{11}$$

in which the divergence theorem can be applied in the first term of integrand:

$$F(\Phi, \varphi) = \int_{\Gamma_1\cup\Gamma_2\cup\Gamma_3\cup\Gamma_4} \hat{\mathbf{n}} \cdot \left(\frac{1}{\rho}\varphi\nabla\Phi\right)d\Gamma + \int_\Omega \left[-\frac{1}{\rho}\nabla\varphi \cdot \nabla\Phi + \varphi\frac{\omega^2}{(\lambda + 2\mu)}\Phi\right]d\Omega = 0. \tag{12}$$

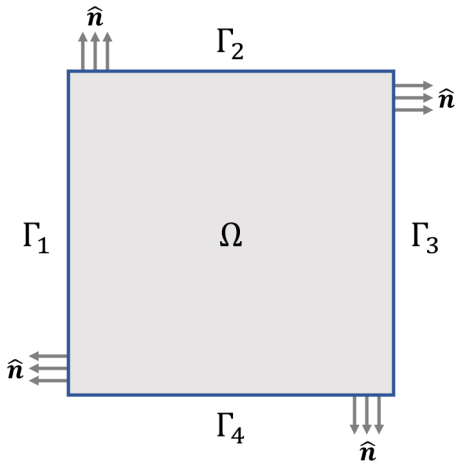

FIG. 2. Schematic of a system composed of the domain Ω and the boundary Γ $(= \Gamma_1 \cup \Gamma_2 \cup \Gamma_3 \cup \Gamma_4)$ with a unit vector $\hat{\mathbf{n}}$ which is outward normal to each boundary.

Here, we suppose that the Dirichlet ($\Phi = 1$) and the Neumann [$\hat{\mathbf{n}} \cdot (\nabla\Phi) = 0$] conditions, which are exactly the same conditions as in Eqs. (7a)–(7d), are imposed on Γ_1 and $\Gamma_2 \cup \Gamma_3 \cup \Gamma_4$, respectively [Fig. 2]. Since $\hat{\mathbf{n}} \cdot (\nabla\Phi) = 0$ on $\Gamma_2 \cup \Gamma_3 \cup \Gamma_4$, the integrals on those boundaries vanish. Therefore, only the integral by the inhomogeneous Dirichlet condition on Γ_1 remains. Then Eq. (12) reduces to

$$F(\Phi, \varphi) = \int_{\Gamma_1} \hat{\mathbf{n}} \cdot \left(\frac{1}{\rho}\varphi\nabla\Phi\right)d\Gamma + \int_\Omega \left[-\frac{1}{\rho}\nabla\varphi \cdot \nabla\Phi + \varphi\frac{\omega^2}{(\lambda + 2\mu)}\Phi\right]d\Omega = 0, \tag{13}$$

where the functional F is subject to those boundary conditions, and the displacement field of the *P*-wave is defined as $u_p = \nabla\Phi$. In the same way, the weak variational form of the *S*-wave in Eq. (9) can be formulated by introducing a functional G as

$$G(u_s, \varphi) = \int_{\Gamma_4} \hat{\mathbf{n}} \cdot \left(\frac{1}{\rho}\varphi\nabla u_s\right)d\Gamma + \int_\Omega \left[-\frac{1}{\rho}\nabla\varphi \cdot \nabla u_s + \varphi\frac{\omega^2}{\mu}u_s\right]d\Omega = 0. \tag{14}$$

We use the "weak form PDE" interface as an ad hoc finite element simulation in COMSOL to compute Eqs. (13) and (14) for seismic waves. When computing the equations, a mesh generation should properly be considered to ensure accurate weak solutions. All results in this study are estimated along the appropriate assigned mesh. For instance, we evaluate Φ of the *P*-wave in soil with the properties: $\nu = 0.3$ (Poisson's ratio), $E = 0.153$ GPa (Young's modulus), $\rho = 1800$ kg/m^3, and $L = L_x = L_y = 5$ m. We also take the modulus conversion formula for homogeneous isotropic matter to obtain λ and μ

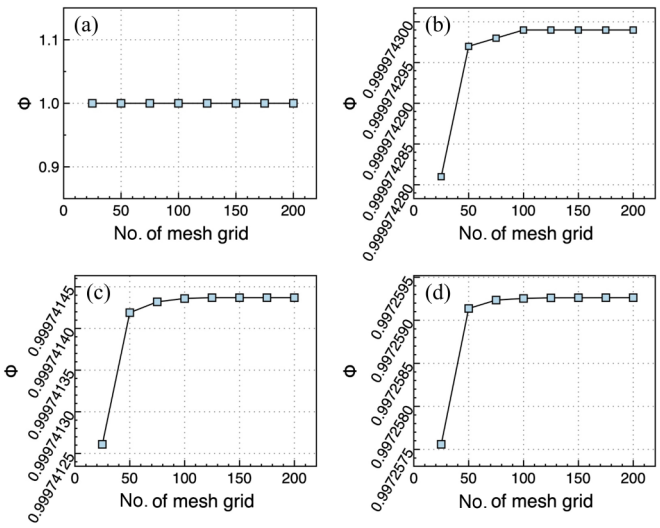

FIG. 3. Mesh convergence of the solution Φ according to the number (No.) of mesh grids at (a) $\epsilon = 0$ m, (b) $\epsilon = 10^{-4}$ m, (c) $\epsilon = 10^{-3}$ m, (d) $\epsilon = 10^{-2}$ m away from the Γ_1 at 100 Hz.

as

$$\lambda = \frac{E\nu}{(1+\nu)(1-2\nu)}, \tag{15a}$$

$$\mu = \frac{E}{2(1+\nu)}. \tag{15b}$$

Hence, with the assigned conditions and properties in Eq. (14), we impose the mapped meshing in Ω and the boundary layer meshing on Γ, and seek the displacements fields. The mesh generation establishes well that the solutions converge to the value (1 m) prescribed by the Dirichlet condition at a location ϵ which is away from the boundary Γ_1 (Fig. 3). At the frequency 100 Hz as an example, Γ_1 with small numbers ($\epsilon =$ 0 m, 10^{-4} m, 10^{-3} m, and 10^{-2} m) shows a fine numerical stability. The number of mesh grids is obtained by counting the numbers of grid lines along the boundary (not the entire domain), as estimated from 25 to 200 with a step of 25. Also, the solution u_s as well as Φ converges to the value (1 m) at other frequencies. Following the generation of appropriate mesh, the obtained numerical solutions for Φ, u_p ($= \nabla\Phi$), and u_s agree well with analytic solutions at 20 to 40 Hz (Fig. 4). In particular, we take $\frac{\partial(*)}{\partial x}\hat{\mathbf{e}}_x + \frac{\partial(*)}{\partial y}\hat{\mathbf{e}}_y$ instead of ∇ during the computation because it considers a 2D system in which $*$ is any solution such as Φ and u_y even though the Del operator is specified in all mathematical expressions. The numerical method that uses the weak formulation is reliable, so we adopt it in the subsequent section that considers band structure in seismic phononic crystals to achieve wave vector k, rather than the potential or displacement field.

III. BAND STRUCTURES AND PROPERTIES FOR SEISMIC PHONONIC CRYSTALS

A. Weak-form-based band structure

So far we have investigated several solutions that arise from the elastodynamic Navier equation, and found that numerical

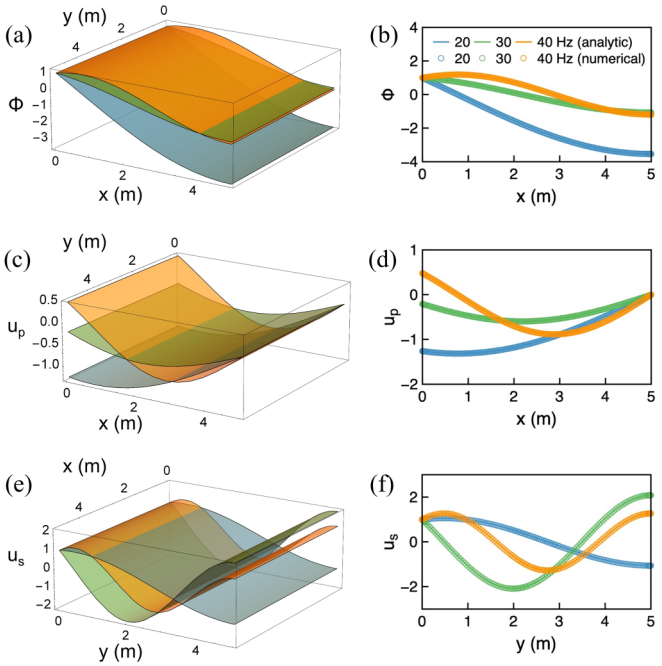

FIG. 4. Solutions of (a) and (b) Φ, (c) and (d) u_p ($= \nabla\Phi$), and (e) and (f) u_s. Left-hand panel indicates each analytic solution in 2D space compared to corresponding numerical solutions on the right-hand side at 20 Hz, 30 Hz, and 40 Hz.

solutions by weak formulation are trustworthy in comparison with analytic solutions. However, the formulas [Eqs. (13) and (14)] must be modified with respect to wave vector $\boldsymbol{k}$ in order that seismic phononic crystals should be analyzed for band structures. Periodically arranged inclusions are embedded in the phononic crystal medium; therefore, we can apply the Floquet-Bloch theorem as

$$F(u_p', \varphi') = \int_\Omega \Big[-\frac{1}{\rho}(-ik+\nabla)\varphi' \cdot (ik+\nabla)u_p' + \varphi' \frac{\omega^2}{(\lambda+2\mu)} u_p' \Big] d\Omega = 0, \tag{16a}$$

$$G(u_s', \varphi') = \int_\Omega \Big[-\frac{1}{\rho}(-ik+\nabla)\varphi' \cdot (ik+\nabla)u_s' + \varphi' \frac{\omega^2}{\mu} u_s' \Big] d\Omega = 0, \tag{16b}$$

where $u_p = \nabla\Phi = u_p' e^{ik\cdot r}$, $u_s = u_s' e^{ik\cdot r}$, and $\varphi = \varphi' e^{-ik\cdot r}$ are assigned. $(\cdot)'$ denotes the periodicity as a Bloch function that satisfies $(\cdot)'(r) = (\cdot)'(r+a)$ for translational symmetry in which r is a position vector and a is a translational vector. Here, a can be expressed as $\frac{2\pi}{L}(n_x, n_y, n_z)^T \in \mathbb{R}^3$ where the real-valued n is determined depending on critical points of the primitive cell in reciprocal space. Then Eqs. (16a) and (16b) represent the $\boldsymbol{k}$ eigenvalue problem to be solved in free space, constrained by Neumann conditions $[\hat{\mathbf{n}} \cdot (\nabla u) = 0]$ for all boundaries. Thus, the integral part over the boundary has been vanished by setting it to be zero, and it enforces a slope continuity of the component u in an outward normal direction on external boundaries. To assure the periodicity

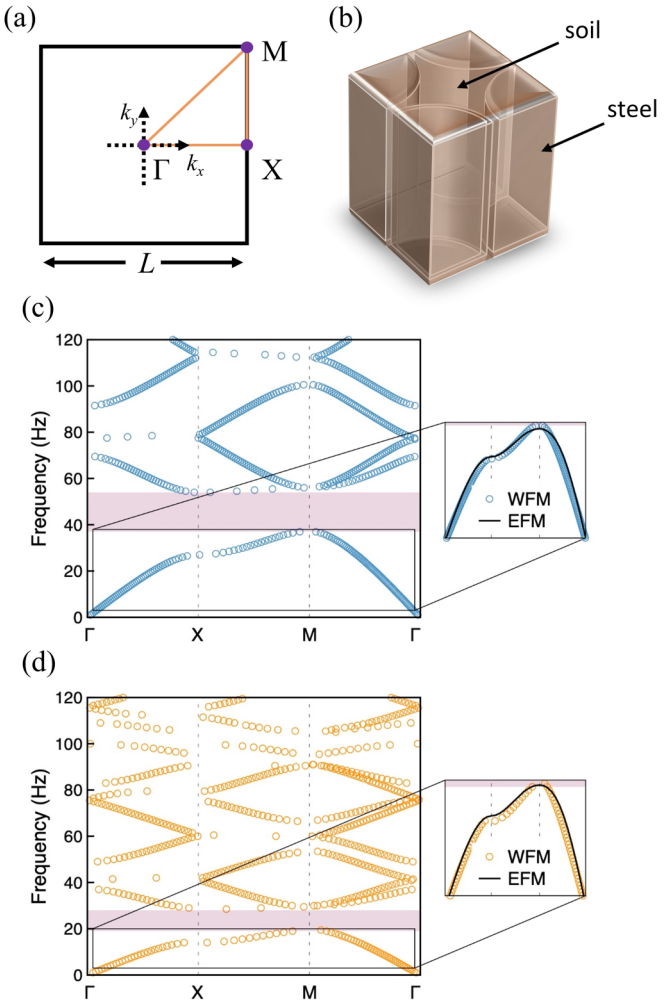

FIG. 5. (a) Schematic of the system based on the square lattice with high symmetry points and lines with respect to reciprocal space. (b) Schematic of the model as a single unit cell composed of steel columns and soil background. Band structures along high symmetry lines for the (c) *P*-wave and (d) *S*-wave. Red region: complete band gap caused by Bragg scattering. Magnified image demonstrates that weak formulation method (WFM) gives the same results as the equifrequency method (EFM).

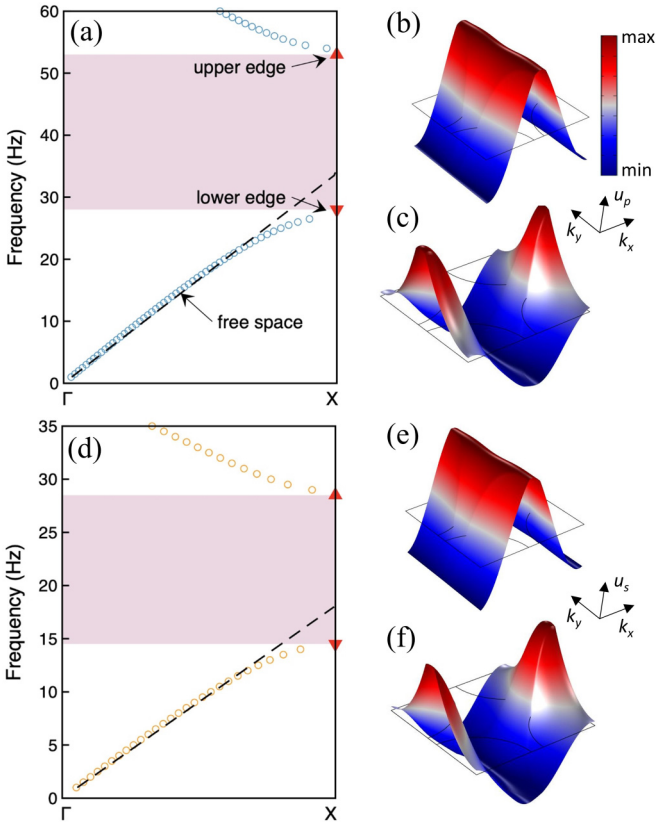

FIG. 6. Reduced Brillouin zone scheme for Γ to X, and eigenmodes at upper and lower edges according to the obtained eigenvalues. Reduced Brillouin zone for the (a) *P*-wave and (d) *S*-wave. Black dashed line: a dispersion curve in the case of free space only with soil background; red triangle: lower and upper edges. Displacement fields for the *P*-wave at (b) the lower edge (at 27 Hz) with eigenvalue $1 + 0.0073193i$ and (c) upper edge (at 53.5 Hz) with eigenvalue $1 - 0.099831i$. Displacement fields for the *S*-wave at (e) lower edge (at 14.5 Hz) with eigenvalue $1 - 0.050357i$ and (f) upper edge (at 28.5 Hz) with eigenvalue $1 + 0.11834i$.

of u, the periodic boundary condition is employed on inlet and outlet boundaries that override the Neumann condition. For an internal boundary in between two domains of the host-inclusion system, the displacement continuity condition ($u^+ = u^-$) is imposed along the surface where the symbols + and − indicate the opposite sides of the internal boundary. Depending on appropriate symmetry lines on the square lattice in this study, we can obtain the information of $\boldsymbol{k}$ with given frequencies. The symmetry points were placed considering the reciprocal lattice [Fig. 5(a)], and the schematic of our model is considered of steel columns and soil background [Fig. 5(b)]. Material properties of the steel column have $\nu = 0.28$ and $E = 200$ GPa with radius $r = 2.25$ m. Given the information about $\boldsymbol{k}$, we can reconstruct band structures of the *P*-wave [Fig. 5(c)] and *S*-wave [Fig. 5(d)] along the high symmetry lines for the real component of wave vector Re($\boldsymbol{k}$). In both cases, Bragg scattering within seismic phononic crystals generates a complete band in which Re($\boldsymbol{k}$) is absent [Figs. 5(c) and 5(d), red area]. In addition, comparison of the results obtained by the weak formulation method agree well with results obtained using the equifrequency method [Figs. 5(c) and 5(d), magnified image]. The complete band gap is generated in a lower frequency range for the *S*-wave than for the *P*-wave due to the restriction of particle velocity (i.e., $c_p > c_s$). Moreover, in the reduced Brillouin zone scheme in Γ-X [Figs. 6(a) and 6(d)], the dispersion curve in free space (black dashed line) is well organized and agrees with the obtained values of Re($\boldsymbol{k}$) until the X point, at which the band gap opens. The eigenmodes of displacement fields for both the *P*- and *S*-wave are also computed at upper and lower edges at the X point along the corresponding eigenvalues [Figs. 6(b) and 6(c), and 6(e) and (f)].

B. Behavior of seismic phononic crystals in band gap

Using the previously analyzed data with the same design as in Fig. 5, we periodically arranged the replicas to examine the wave propagation dynamics in the band gap. The *P*-wave

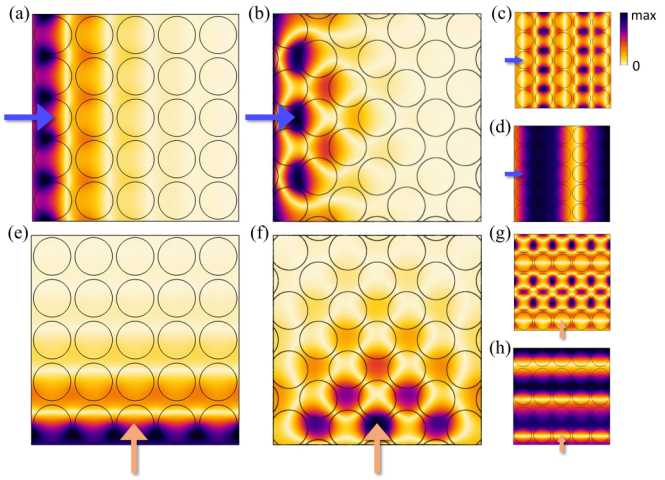

FIG. 7. Displacement fields of periodically arranged seismic phononic crystals. Excitations of the *P*-wave at 45 Hz by (a) plane wave and (b) 45°-tilted wave in band gap; (c) at 60 Hz out of band gap, and (d) at 10 Hz out of band gap. Excitations of *S*-wave at 20 Hz by (e) plane wave and (f) 45°-tilted wave in band gap, and by (g) 35 Hz and (h) 10 Hz out of band gap.

cannot pass through the crystals in the x-direction in the band gap at 45 Hz, because the waves have no propagation mode [Fig. 7(a)], whereas the waves do propagate at 60 Hz [Fig. 7(c)] and 10 Hz [Fig. 7(d)]. Moreover, because of the complete band gap, any oblique incident waves are also forbidden within the crystals. Therefore, the result for the 45°-tilted wave at 45 Hz is the same as for the normal-incident wave [Fig. 7(b)]. The behavior of the *S*-wave in the y-direction within crystals is also the same as that of the *P*-wave.

For practical reasons, the seismic phononic crystals should be as thin as possible in a lateral direction. In order to achieve this miniaturized structure, the "propagation length" or "skin depth", which is widely used in surface plasmon polariton, should be investigated in a similar way. The analogy of phononic crystals is preserved because evanescent modes instead of propagation modes occur in band gaps. Therefore, if we assume that a wave that propagates in the x-direction has an exponential decaying component in band gaps, one can be expressed as

$$\begin{aligned} u &= u_0 e^{i(\mathrm{Re}(k_x)x + i\,\mathrm{Im}(k_x)x)} \\ &= u_0 e^{i|\mathrm{Re}(k_x)||x|} e^{-|\mathrm{Im}(k_x)||x|}, \end{aligned} \tag{17}$$

where the imaginary term determines the propagation length as

$$l_p = \frac{1}{|\mathrm{Im}(k_x)|}, \tag{18}$$

where l_p denotes the distance for the absolute displacement field to decay by a factor of $1/e$. Due to internal Bragg scattering, aseismic waves within phononic crystal medium cannot propagate in band gaps. The medium has only evanescent modes [Im(k)], but no propagation modes [Re(k)], so it can be considered to be a locally evanescent regime. Our approach yields a complex-valued k, so l_p can be evaluated. Therefore, we explicitly obtain the maximum propagation lengths in the entire frequency range of the band gap regime;

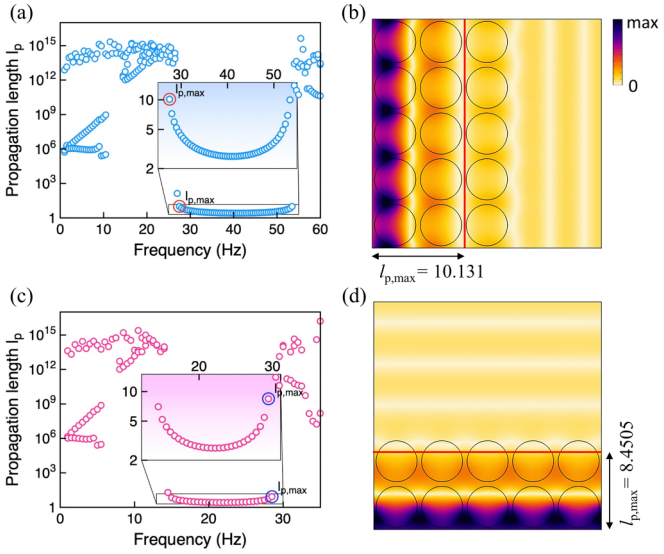

FIG. 8. Propagation length along frequency, and redesigned seismic phononic crystals following the maximum propagation length in the band gap region. (a) and (c) indicate that l_p in the band gap regime is a sufficiently predictable variable (magnified image) of *P*- and *S*-waves. (b) and (d) are the rearrangements of miniaturized phononic crystals for *P*- and *S*-waves, resulting in adequate band gap phenomena.

the results were $l_{p,\mathrm{max}} = 10.131$ m for the *P*-wave [Fig. 8(a)] and $l_{p,\mathrm{max}} = 8.4505$ m for the *S*-wave [Fig. 8(c)]. Such information enables us to redesign phononic crystals to be as thin as possible in a lateral direction, because the length of the whole crystal that exceeds propagation length is not necessary anymore for practical usage. Here, we rearrange seismic phononic crystals from *P*- and *S*-waves, and the length of miniaturized crystal L_m is subject to restriction $L_m = [(l_{p,\mathrm{max}} + L)/L] \times L \leqslant l_{p,\mathrm{max}} + L$, where $[\cdots]$ is the largest integer that is less than or equal to $\cdots$ [Figs. 8(b) and 8(d)]. The minimized structures work well in band gaps at 45 Hz and 20 Hz as expected.

C. Material property dependency on propagation length

We also investigated the dependency of particle velocity on varying mass densities ($\rho = [1.8 \times 10^3,\ 8 \times 10^5]$ kg/m^3) while obtaining the complex-valued effective particle velocity by a parametric study of mass density, while maintaining the same $\nu = 0.3$, $E = 0.153$ GPa as the soil background. The effective particle velocity is defined as

$$c_{\mathrm{eff}} = 1/n_{\mathrm{eff}} = k_b/k_{\mathrm{eff}}, \tag{19}$$

where $k_b = \omega/c_b$ and $\omega = 2\pi f$, and the effective refractive index n_{eff} is the inverse of c_{eff}. c_b is determined differently for *P*- and *S*-waves. Preserving $f = 45$ Hz for the *P*-wave, and $f = 20$ Hz for the *S*-wave, the lossy component of c_{eff} becomes the dominant factor for hard materials (high mass density) and yields precise low l_p still in the band gap [Fig. 9(a)], whereas no lossy component of c_{eff} occurs in soft materials (low mass density) so they have extremely high l_p that does not occur in the band gap [Fig. 9(b)]. In addition, mechanical properties for several materials (Table I) were used for data

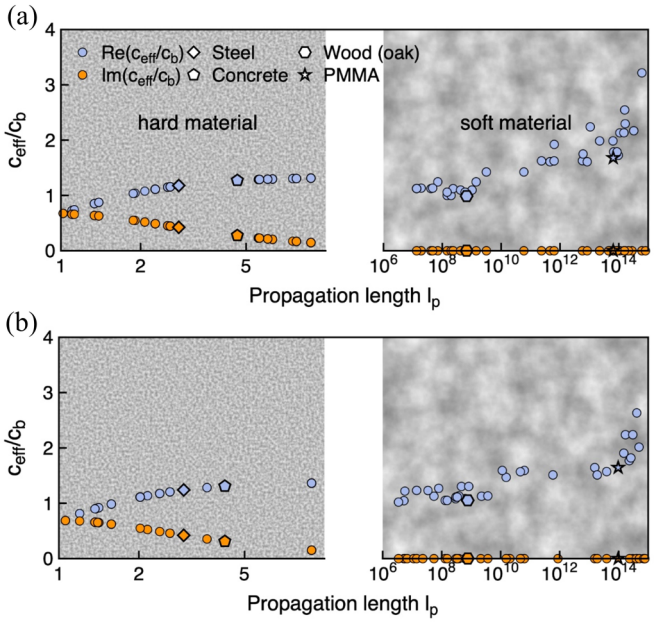

FIG. 9. c_{eff}/c_b along l_p. Hard materials (left region) such as steel and concrete with high mass density generate low l_p induced by occurrence of $\text{Im}(c_{\text{eff}}/c_b)$. On the other hand, soft materials (right region) such as wood (oak) and PMMA with low mass density generate extremely high l_p without any disturbance of $\text{Im}(c_{\text{eff}}/c_b)$.

in Fig. 9 as reference. For hard materials, seismic waves weakly experience propagation modes, but instead experience evanescent modes induced by multiple scattering between inclusions within the medium; this phenomenon yields a band gap that arises from $\text{Im}(\boldsymbol{k})$. However, for soft materials, the waves strongly experience propagation modes in that medium and still propagate through the crystals with no reflection.

D. Depth effect in three-dimensional system

Until now, all analyses of seismic phononic crystals have entirely been done with a 2D model. In this case, the depth of the 2D model on the z-axis is regarded as an infinitely long height. However, in real systems, the depth must be finite and therefore the effect of it is the primary consideration. Following the concern, we added two domains at the top and bottom of phononic crystals (main domain) with perfectly matched layers (PMLs) in Fig. 10(a). PMLs have been imposed to reduce unwanted numerical reflections on interfaces. For both

TABLE I. Several mechanical material properties used in Fig. 9. It is expected to distinguish which material effectively belongs to a hard material with given single frequency regarding the propagation length.

Materials	Mass density (ρ)	Young's modulus (E)	Poisson's ratio (ν)
Steel	8000 kg/m^3	200 GPa	0.28
Concrete	2400	30	0.15
Wood (oak)	720	6.1	0.37
PMMA	1180	3.2	0.35

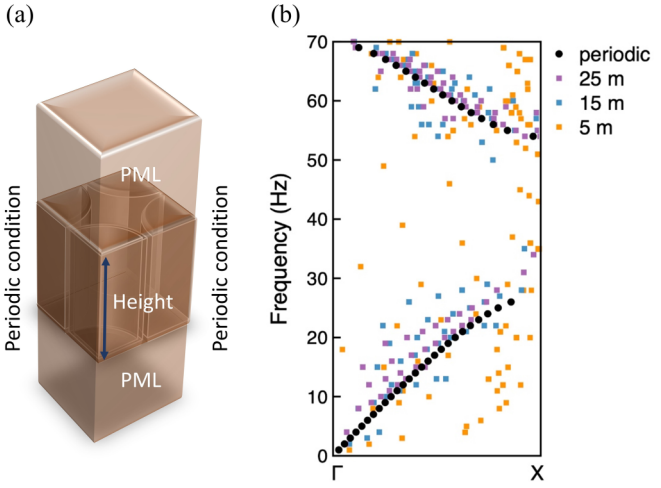

FIG. 10. (a) Three-dimensional (3D) computational schematic domains. The seismic phononic crystals (main domain) is embedded in between two PMLs with the variable h, and have periodic boundary conditions at both sides. (b) Reduced Brillouin zone scheme of the P-wave in 3D space. $\text{Re}(k_x)$ with respect to h steadily converge to the obtained values when the periodic condition rather than finite h is considered.

sides of the main domain on the x- and y-axes, periodic conditions have been imposed the same as in the 2D model. Reduced Brillouin zone of the P-wave shows that the depth h of seismic phononic crystals should be at least $h \geqslant 4 \times L$ [Fig. 10(b)] to ensure that $\text{Re}(k_x)$ with finite h converges to the case when the periodic condition is imposed on the z-axis.

IV. CONCLUSION

In summary, we have investigated seismic phononic crystals driven by an elastodynamic Navier equation. From the consistent values of the potential and displacement fields by analytic and numerical approaches, the numerical analysis via weak formulation method shows a satisfactory stability. Using the proposed method, we have analyzed band structures of seismic phononic crystals with cylindrical steel inclusions and soil background, and observed complete band gaps for the P- and S-waves. Moreover, utilizing the propagation length by information of complex-valued wave vector, we showed the feasibility of miniaturized seismic phononic crystals for practical usage. Also, we have shown how the relation between effective particle velocity and propagation length is affected by evaluating material property. Furthermore, three-dimensional analysis for depth effect of phononic crystals has been conducted showing that the depth should be at least larger than 4 times by lattice constant. With the presented work, we hope that this understanding of wave propagation in periodic composites will be used to develop seismic-resistant construction materials. These future-oriented manmade structures can potentially be buried beneath the ground surrounding regions such as nuclear power station, geothermal power plant, and electricity pylon that should be isolated from an unexpected state.

ACKNOWLEDGMENTS

This work was financially supported by the K-Cloud (Grant No. 2018-TECH-04) funded by the Korea Hydro & Nuclear Power Co. Ltd. This work was also partially supported by the National Research Foundation of Korea (NRF) (Grants No. NRF-2019R1A2C3003129, No. CAMM-2019M3A6B3030637, No. NRF-2019R1A5A8080290, No. NRF-2018M3D1A1058998, and No. NRF-2015R1A5A1037668) funded by the Ministry of Science and ICT (MSIT) of the Korean government. D.L. acknowledges support for the Global Ph.D. Fellowship (NRF-2018H1A2A1062053) from NRF-MSIT of the Korean government.

[1] V. Veselago, Usp. Fiz. Nauk **92**, 517 (1967).
[2] D. R. Smith, W. J. Padilla, D. C. Vier, S. C. Nemat-Nasser, and S. Schultz, Phys. Rev. Lett. **84**, 4184 (2000).
[3] J. B. Pendry, Phys. Rev. Lett. **85**, 3966 (2000).
[4] X. Ni, Z. J. Wong, M. Mrejen, Y. Wang, and X. Zhang, Science **349**, 1310 (2015).
[5] B. Orazbayev, N. Mohammadi Estakhri, M. Beruete, and A. Alù, Phys. Rev. B **91**, 195444 (2015).
[6] Y. Yang, L. Jing, B. Zheng, R. Hao, W. Yin, E. Li, C. M. Soukoulis, and H. Chen, Adv. Mater. **28**, 6866 (2016).
[7] B. Orazbayev, N. Mohammadi Estakhri, A. Alù, and M. Beruete, Adv. Opt. Mater. **5**, 1600606 (2017).
[8] M. Bayindir, B. Temelkuran, and E. Ozbay, Appl. Phys. Lett. **77**, 3902 (2000).
[9] B.-S. Song, S. Noda, and T. Asano, Science **300**, 1537 (2003).
[10] T. D. Happ, M. Kamp, A. Forchel, J.-L. Gentner, and L. Goldstein, Appl. Phys. Lett. **82**, 4 (2003).
[11] H. Němec, L. Duvillaret, F. Garet, P. Kužel, P. Xavier, J. Richard, and D. Rauly, J. Appl. Phys. **96**, 4072 (2004).
[12] Y. Sugimoto, Y. Tanaka, N. Ikeda, Y. Nakamura, K. Asakawa, and K. Inoue, Opt. Express **12**, 1090 (2004).
[13] N. Skivesen, A. Têtu, M. Kristensen, J. Kjems, L. H. Frandsen, and P. I. Borel, Opt. Express **15**, 3169 (2007).
[14] M. Farhat, S. Guenneau, and S. Enoch, Phys. Rev. Lett. **103**, 024301 (2009).
[15] S. Brûlé, E. H. Javelaud, S. Enoch, and S. Guenneau, Phys. Rev. Lett. **112**, 133901 (2014).
[16] A. Colombi, P. Roux, S. Guenneau, P. Gueguen, and R. V. Craster, Sci. Rep. **6**, 19238 (2016).
[17] A. Colombi, P. Roux, and M. Rupin, J. Acoust. Soc. Am. **136**, EL192 (2014).
[18] E. G. Williams, P. Roux, M. Rupin, and W. A. Kuperman, Phys. Rev. B **91**, 104307 (2015).
[19] D. Colquitt, A. Colombi, R. Craster, P. Roux, and S. Guenneau, J. Mech. Phys. Solids **99**, 379 (2017).
[20] P. Roux, D. Bindi, T. Boxberger, A. Colombi, F. Cotton, I. Douste-Bacque, S. Garambois, P. Gueguen, G. Hillers, D. Hollis *et al.*, Seismol. Res. Lett. **89**, 582 (2018).
[21] B. Ungureanu, Y. Achaoui, S. Brule, S. Enoch, R. Craster, and S. Guenneau, arXiv:1904.10767 (2018).
[22] S. Brûlé, S. Enoch, and S. Guenneau, arXiv:1904.05323 (2019).
[23] B. Ungureanu, S. Guenneau, Y. Achaoui, A. Diatta, M. Farhat, H. Hutridurga, R. V. Craster, S. Enoch, and S. Brûlé, arXiv:1904.04133 (2019).
[24] S. Brule, S. Enoch, and S. Guenneau, arXiv:1809.05841 (2018).
[25] D. Lee, M. Kim, and J. Rho, J. Phys. Condens. Matter **31**, 375901 (2019).
[26] D. C. Dobson, J. Gopalakrishnan, and J. E. Pasciak, J. Comput. Phys. **161**, 668 (2000).
[27] Y. Liu and L.-t. Gao, Solid State Commun. **144**, 89 (2007).
[28] J. Li, Y.-S. Wang, and C. Zhang, in *2008 IEEE Ultrasonics Symposium* (IEEE, Beijing, China, 2008), pp. 1468–1471.
[29] J. Li, Y.-S. Wang, and C. Zhang, in *Proceedings of the Second International Symposium on Computational Mechanics and the 12th International Conference on the Enhancement and Promotion of Computational Methods in Engineering and Science*, edited by J. W. Z. Lu, A. Y. T. Leung, V. Pan Iu, and K. M. Mok, AIP Conf. Proc. No. 1233 (AIP, Melville, NY, 2010), pp. 131–136.
[30] L. Landau, E. Lifshitz, A. Kosevich, J. Sykes, L. Pitaevskii, and W. Reid, *Theory of Elasticity*, Course of Theoretical Physics (Elsevier Science, New York, 1986).
[31] K. Graff, *Wave Motion in Elastic Solids*, Dover Books on Physics (Dover Publications, 1991).
[32] K. Aki and P. G. Richards, *Quantitative Seismology* (University Science Books, 2002).
[33] H. Helmholtz, J. Reine Angew. Math. **55**, 25 (1858).